ALMA SPECTROSCOPIC SURVEY IN THE HUBBLE ULTRA DEEP FIELD: SURVEY DESCRIPTION

Fabian Walter[1,2,3], Roberto Decarli[1], Manuel Aravena[4], Chris Carilli[3,5], Rychard Bouwens[6], Elisabete da Cunha[7,8], Emanuele Daddi[9], R. J. Ivison[10,11], Dominik Riechers[12], Ian Smail[13], Mark Swinbank[13], Axel Weiss[14], Timo Anguita[15,16], Roberto Assef[4], Roland Bacon[17], Franz Bauer[18,19,20], Eric F. Bell[21], Frank Bertoldi[22], Scott Chapman[23], Luis Colina[24], Paulo C. Cortes[25,26], Pierre Cox[27], Mark Dickinson[27], David Elbaz[9], Jorge Gónzalez-López[18], Edo Ibar[28], Hanae Inami[17], Leopoldo Infante[18], Jacqueline Hodge[6], Alex Karim[22], Olivier Le Fevre[29], Benjamin Magnelli[22], Roberto Neri[30], Pascal Oesch[31], Kazuaki Ota[5,32], Gergö Popping[10], Hans-Walter Rix[1], Mark Sargent[33], Kartik Sheth[34], Arjen van der Wel[1], Paul van der Werf[6], and Jeff Wagg[35]

[1] Max-Planck Institut für Astronomie, Königstuhl 17, D-69117, Heidelberg, Germany; walter@mpia.de
[2] Astronomy Department, California Institute of Technology, MC105-24, Pasadena, CA 91125, USA
[3] National Radio Astronomy Observatory, Pete V. Domenici Array Science Center, P.O. Box O, Socorro, NM 87801, USA
[4] Núcleo de Astronomía, Facultad de Ingeniería, Universidad Diego Portales, Av. Ejército 441, Santiago, Chile
[5] Cavendish Laboratory, University of Cambridge, 19 J J Thomson Avenue, Cambridge CB3 0HE, UK
[6] Leiden Observatory, Leiden University, P.O. Box 9513, NL2300 RA Leiden, The Netherlands
[7] Centre for Astrophysics and Supercomputing, Swinburne University of Technology, Hawthorn, Victoria 3122, Australia
[8] Research School of Astronomy and Astrophysics, Australian National University, Canberra, ACT 2611, Australia
[9] Laboratoire AIM, CEA/DSM-CNRS-Universite Paris Diderot, Irfu/Service d'Astrophysique, CEA Saclay, Orme des Merisiers, F-91191 Gif-sur-Yvette cedex, France
[10] European Southern Observatory, Karl-Schwarzschild-Strasse 2, D-85748, Garching, Germany
[11] Institute for Astronomy, University of Edinburgh, Royal Observatory, Blackford Hill, Edinburgh EH9 3HJ, UK
[12] Cornell University, 220 Space Sciences Building, Ithaca, NY 14853, USA
[13] 6 Centre for Extragalactic Astronomy, Department of Physics, Durham University, South Road, Durham, DH1 3LE, UK
[14] Max-Planck-Institut für Radioastronomie, Auf dem Hügel 69, D-53121 Bonn, Germany
[15] Departamento de Ciencias Físicas, Universidad Andres Bello, Fernandez Concha 700, Las Condes, Santiago, Chile
[16] Millennium Institute of Astrophysics, Chile
[17] Université Lyon 1, 9 Avenue Charles André, F-69561 Saint Genis Laval, France
[18] Instituto de Astrofísica, Facultad de Física, Pontificia Universidad Católica de Chile Av. Vicuña Mackenna 4860, 782-0436 Macul, Santiago, Chile
[19] Millennium Institute of Astrophysics (MAS), Nuncio Monseñor Sótero Sanz 100, Providencia, Santiago, Chile
[20] Space Science Institute, 4750 Walnut Street, Suite 205, Boulder, CO 80301, USA
[21] Department of Astronomy, University of Michigan, 1085 South University Avenue, Ann Arbor, MI 48109, USA
[22] Argelander Institute for Astronomy, University of Bonn, Auf dem Hügel 71, D-53121 Bonn, Germany
[23] Dalhousie University, Halifax, Nova Scotia, Canada
[24] ASTRO-UAM, UAM, Unidad Asociada CSIC, Spain
[25] Joint ALMA Observatory—ESO, Av. Alonso de Córdova, 3104, Santiago, Chile
[26] National Radio Astronomy Observatory, 520 Edgemont Road, Charlottesville, VA 22903, USA
[27] Steward Observatory, University of Arizona, 933 N. Cherry Street, Tucson, AZ 85721, USA
[28] Instituto de Física y Astronomía, Universidad de Valparaíso, Avda. Gran Bretaña 1111, Valparaiso, Chile
[29] Aix Marseille Universite, CNRS, LAM (Laboratoire d'Astrophysique de Marseille), UMR 7326, F-13388 Marseille, France
[30] IRAM, 300 rue de la piscine, F-38406 Saint-Martin d'Hères, France
[31] Astronomy Department, Yale University, New Haven, CT 06511, USA
[32] Kavli Institute for Cosmology, University of Cambridge, Madingley Road, Cambridge CB3 0HA, UK
[33] Astronomy Centre, Department of Physics and Astronomy, University of Sussex, Brighton, BN1 9QH, UK
[34] NASA Headquarters, Washington DC, 20546-0001, USA
[35] SKA Organization, Lower Withington Macclesfield, Cheshire SK11 9DL, UK

ABSTRACT

We present the rationale for and the observational description of ASPECS: the ALMA SPECtroscopic Survey in the *Hubble* Ultra-Deep Field (UDF), the cosmological deep field that has the deepest multi-wavelength data available. Our overarching goal is to obtain an unbiased census of molecular gas and dust continuum emission in high-redshift ($z > 0.5$) galaxies. The $\sim 1'$ region covered within the UDF was chosen to overlap with the deepest available imaging from the *Hubble Space Telescope*. Our ALMA observations consist of full frequency scans in band 3 (84–115 GHz) and band 6 (212–272 GHz) at approximately uniform line sensitivity ($L'_{CO} \sim 2 \times 10^9$ K km s^{-1} pc^2), and continuum noise levels of 3.8 μJy beam^{-1} and 12.7 μJy beam^{-1}, respectively. The molecular surveys cover the different rotational transitions of the CO molecule, leading to essentially full redshift coverage. The [C II] emission line is also covered at redshifts $6.0 < z < 8.0$. We present a customized algorithm to identify line candidates in the molecular line scans and quantify our ability to recover artificial sources from our data. Based on whether multiple CO lines are detected, and whether optical spectroscopic redshifts as well as optical counterparts exist, we constrain the most likely line identification. We report 10 (11) CO line candidates in the 3 mm (1 mm) band, and our statistical analysis shows that <4 of these (in each band) are likely spurious. Less than one-third of the total CO flux in the low-J CO line candidates are from sources that are not associated with an optical/NIR counterpart. We also present continuum maps of both the band 3 and band 6 observations. The data presented here form the basis of a number of dedicated studies that are presented in subsequent papers.

Key words: galaxies: evolution – galaxies: ISM – galaxies: high-redshift – galaxies: formation – surveys

1. INTRODUCTION

Characterizing the molecular gas content of distant galaxies is essential in order to understand the evolution of the cosmic star-formation rate density (Madau & Dickinson 2014), and the build-up of stellar mass (Bell et al. 2003) throughout cosmic time (Carilli & Walter 2013). A unique way to fully characterize the molecular gas content in galaxies in the early universe is through spectral line scans in well-studied cosmological deep fields. In comparison to targeted observations of individual galaxies, spectral scans have the advantage that molecular gas reservoirs can be characterized without pre-selection through other information (e.g., stellar mass, star-formation rate). Such spectral line scans can also potentially reveal the presence of gas-rich "dark" galaxies, i.e., galaxies that are invisible in the optical wavebands, and that would not be selected as targets to search for molecular gas emission (e.g., Walter et al. 2012). In a sense, spectral line scans follow the spirit of the original *Hubble Space Telescope* (*HST*) deep fields (e.g., Williams et al. 1996; Beckwith et al. 2006) because essentially no prior knowledge/selection based on galaxy properties enters the choice of field.

As the main constituent of the molecular gas in galaxies, molecular hydrogen (H_2) is too weak to be detected, the next most abundant tracer is typically used to measure the molecular gas content: ^{12}CO (hereafter: CO). Although this molecule is 10^4 times less abundant, the line can be detected in various environments. As a consequence, this molecule has been used at low and high redshift to measure gas masses and kinematics. The CO line emission is observed in various rotational transitions in galaxies (e.g., Carilli & Walter 2013). The rotational ground-state ($J = 1$–0) of CO is at 115.271 GHz, and the higher rotational states ($J > 1$) are approximately equally spaced by that frequency.[36] The amount of high-J emission depends on the a priori unknown excitation of the molecular gas. Nevertheless, full frequency scans in the lowest frequency ALMA bands cover CO emission at essentially all redshifts (see Figure 1).

In this paper, we present the rationale for, and the observational description of, ASPECS: The ALMA SPECtroscopic Survey in the *Hubble* Ultra-Deep Field (UDF). This paper is structured as follows: Section 2 summarizes our field choices, as well as the observations and data reduction. In Section 3, we describe our methodology to identify line candidates in our data cubes, and present the continuum maps of both the band 3 and band 6 observations. In Section 4, we compare our findings to simple expectations based on previous multi-wavelength analysis of the galaxies in the field. We present our summary in Section 5.

A number of accompanying papers build on the data presented in this paper (hereafter: Paper I). In Paper II (Aravena et al. 2016a), we analyze the continuum information (mostly based on the band 6 observations); in Paper III (Decarli et al. 2016a), we discuss the implications for CO luminosity functions and the redshift evolution of the cosmic molecular gas density; in Paper IV (Decarli et al. 2016b), we examine the properties of those galaxies in the UDF that show bright CO emission; in Paper V (Aravena et al. 2016b), we search for [C II] emitters; in Paper VI (Bouwens et al. 2016), we investigate where high-redshift galaxies from ASPECS lie in
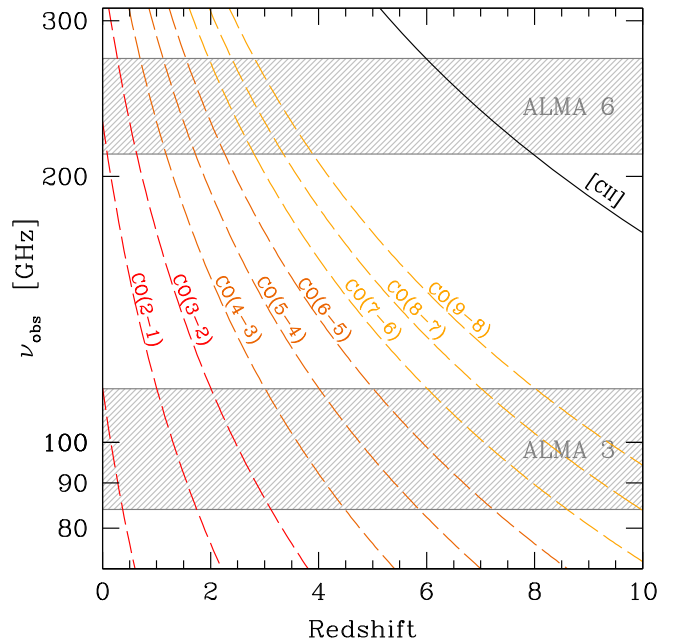

Figure 1. CO and [C II] redshift coverage of our molecular line scans at 1 mm and 3 mm. See Table 1 for the exact redshift ranges of each transition. The 1mm+3 mm synergy provides continuous CO redshift coverage at virtually any redshift, with only a tiny gap at $0.6309 < z < 0.6950$. The [C II] emission line is covered in the redshift range of $6 < z < 8$ and is discussed in Paper V.

relation to known IRX-β and IRX-stellar mass relationships, and finally, in Paper VII (Carilli et al. 2016), we describe implications on intensity mapping experiments. Throughout the paper, we assume a standard cosmology with $H_0 = 70 \, km \, s^{-1} \, Mpc^{-1}$, $\Omega_m = 0.3$, and $\Omega_\Lambda = 0.7$, broadly in agreement with the most recent *Planck* measurements (Planck Collaboration XIII 2016). Where required, we refer to the AB photometric system (Oke & Gunn 1983) for the magnitude definitions and to Chabrier (2005) for the stellar initial mass function.

2. OBSERVATIONS AND DATA REDUCTION

2.1. Choice of Frequencies

Given the unknown excitation of the molecular gas in a given high-redshift galaxy, when inferring H_2 masses, it is advantageous to observe the CO emission in the lowest rotational state possible to minimize excitation corrections, modulo the impact of the Cosmic Microwave Background (da Cunha et al. 2013a). With ALMA, the lowest frequencies are accessible in band 3, which therefore is the primary band of choice. An important complement are line scan observations in band 6, as the combination of both bands results in the following: (1) other than one small gap in redshift, there is essentially complete redshift coverage at all redshifts (see Figure 1 and Table 1), (2) the CO excitation (or limits on it) can be immediately constrained through the detection of multiple rotational transitions, (3) deep continuum maps in the respective observing bands are available "for free," and (4) the highest-redshift sources at $6 < z < 8$ can be probed through [C II] emission.

Band 7 (275–373 GHz) observations may be preferred when one is interested only in the continuum flux densities of the galaxies, but such observations would only recover very high J ($J > 6$) transitions at $z > 2$, which may not be highly excited

---

[36] In reality, the spacing changes slightly as the dipole moment changes for the higher transitions as a result of centrifugal forces.

Table 1
Lines and Corresponding Redshift Ranges Covered in the Molecular Line Scans

Transition	ν_0 (GHz)	z_{min}	z_{max}	$\langle z \rangle$	Volume (Mpc^3)
(1)	(2)	(3)	(4)	(5)	(6)
band 3: 3 mm (84.176–114.928 GHz)					
CO(1-0)	115.271	0.0030	0.3694	0.2801	89
CO(2-1)	230.538	1.0059	1.7387	1.4277	1920
CO(3-2)	345.796	2.0088	3.1080	2.6129	3363
CO(4-3)	461.041	3.0115	4.4771	3.8030	4149
CO(5-4)	576.268	4.0142	5.8460	4.9933	4571
CO(6-5)	691.473	5.0166	7.2146	6.1843	4809
CO(7-6)	806.652	6.0188	8.5829	7.3750	4935
[C I]$_{1-0}$	492.161	3.2823	4.8468	4.1242	4287
[C I]$_{2-1}$	809.342	6.0422	8.6148	7.4031	4936
band 6: 1 mm (212.032–272.001 GHz)					
CO(2-1)	230.538	0.0000	0.0873	0.0656	1.4
CO(3-2)	345.796	0.2713	0.6309	0.4858	314
CO(4-3)	461.041	0.6950	1.1744	0.9543	1028
CO(5-4)	576.268	1.1186	1.7178	1.4297	1759
CO(6-5)	691.473	1.5422	2.2612	1.9078	2376
CO(7-6)	806.652	1.9656	2.8044	2.3859	2864
[C I]$_{1-0}$	492.161	0.8094	1.3212	1.0828	1233
[C I]$_{2-1}$	809.342	1.9755	2.8171	2.3973	2875
[C II]$_{3/2-1/2}$	1900.548	5.9873	7.9635	6.9408	4431

Note. For the 3 mm data, comoving volume and volume-weighted average redshifts are computed within the primary beam, accounting for its frequency dependence. For the 1 mm data, the area is fixed (3700 arcsec^2, as set by the size of the final mosaic).

in main-sequence galaxies (Daddi et al. 2015). Also, the field of view is smaller than in band 6, necessitating more extensive mosaicing. The bandwidth of band 7 (~100 GHz) requires more than 13 frequency tunings (each with a bandwidth of 8 GHz). For all of these reasons, band 6 is preferred over band 7 to complement the band 3 observations.

We obtained full frequency scans in both ALMA band 3 and band 6. In band 3, this implied five frequency setups, labelled A–E in Figure 2. Both the upper and lower side band cover 3.75 GHz, with a gap of ~8 GHz. For that reason, the central range in band 3 was covered twice, resulting in observations with lower noise in that frequency window. Such an overlap region did not result from the setup of the band 6 frequency scan because the gap between the upper and lower side band in band 6 is 12 GHz (see right panel in Figure 2). Panels of Figure 2 show the resulting noise as a function of frequency. The noise increase in band 3 toward the higher frequencies is due the atmospheric oxygen line significantly increasing the system temperatures above >113 GHz. As a consequence of the higher frequency, the noise in band 6 observations was significantly higher (and less well-behaved due to skylines etc.) than in band 3.

2.2. Choice of Field

In principle, such molecular line scan observations could be obtained at (almost) any position in the sky that is not affected by foreground emission (either our Galaxy, or other nearby galaxies). However, the analysis and interpretation of the detected galaxies is greatly facilitated if a field is chosen for

which multi-wavelength observations already exist. It also should be a field that is easily accessible to ALMA. The *Hubble* Ultra Deep Field (UDF, Beckwith et al. 2006) is the cosmological field with the deepest observations in all important wavebands, with 18,000 cataloged galaxies (Coe et al. 2006). The UDF is situated in the 30′ Extended *Chandra* Deep Field South (ECDFS Lehmer et al. 2005)/GOODS-South (Giavalisco et al. 2004)/CANDELS (Grogin et al. 2011; Koekemoer et al. 2011) region, so the large-scale structure around this field is well quantified.

The goal of the ALMA frequency scan was to reach a sensitivity such that the predicted "knee" of the CO luminosity function could be reached at $z \sim 2$ (e.g., Sargent et al. 2014). Given that multiple frequency settings were needed to cover both band 3 and band 6, and given the limited amount of time available in ALMA cycle 2, this implied that only the area corresponding to one pointing in band 3 could be covered by our observations. This ~1′ region was covered with a seven-point mosaic in band 6 (see Figure 3). Our pointing was chosen to lie in the deepest part of the UDF, the so-called UDF12 (Ellis et al. 2013) or eXtremely Deep Field (XDF, Illingworth et al. 2013; hereafter: XDF) and included the highest number of z-drop galaxy candidates, i.e., galaxies at $z > 6$, that could be detectable in [C II] emission. The field also comprises a significant overlap with the deepest MUSE observations of the UDF (R. Bacon et al. 2016, in preparation). The region covered by our observations comprises ~10% of the total area of the UDF (corresponding to a comoving survey volume of 18,000 Mpc^3 out to $z \sim 8$) and harbors roughly ~1500 optical/NIR-selected galaxies. In Figure 3, we also present the star-formation rates and stellar masses of all galaxies covered by our observations, based on the fitting of the galaxies' spectral energy distribution (Section 4).

2.3. Choice of Array Configuration

ALMA has been designed to reach high (sub-arcsec) angular resolution. However, to be sensitive to the full molecular gas reservoir in a galaxy, observations in a compact array configuration are essential to ensure that no extended CO emission is missed by the interferometer. Note that this is not related to the "missing short spacing" problem.[37] For instance, in observations with extended ALMA array configurations the synthesized beam will end up being smaller than the typical size of a high-redshift galaxy. As a result, the amount of emission per beam is only a fraction of the total emission of the galaxy, while the noise does not change. In the case of low S/N detections, this will result in the non-detection of a source, whereas the emission would be detected by a compact configuration. Our observations were taken in the C34-2 and C34-1 configurations, resulting in beam sizes of $3''\!.6 \times 2''\!.1$ (band 3) and $1''\!.7 \times 0''\!.9$ (band 6), i.e., well matched to the expected sizes of the galaxies under consideration.

2.4. Observations

The project consists of two spectral scans, one at 3 mm (band 3) covering the frequency range 84–115 GHz and one at 1 mm (band 6) covering the frequency range 212–272 GHz (see

---

[37] The missing short spacing problem means that the interferometer is "blind" to spatial scales above a certain size. Given the likely clumpiness of high-redshift galaxies, missing short spacings should typically not be a concern in high-redshift galaxy observations.
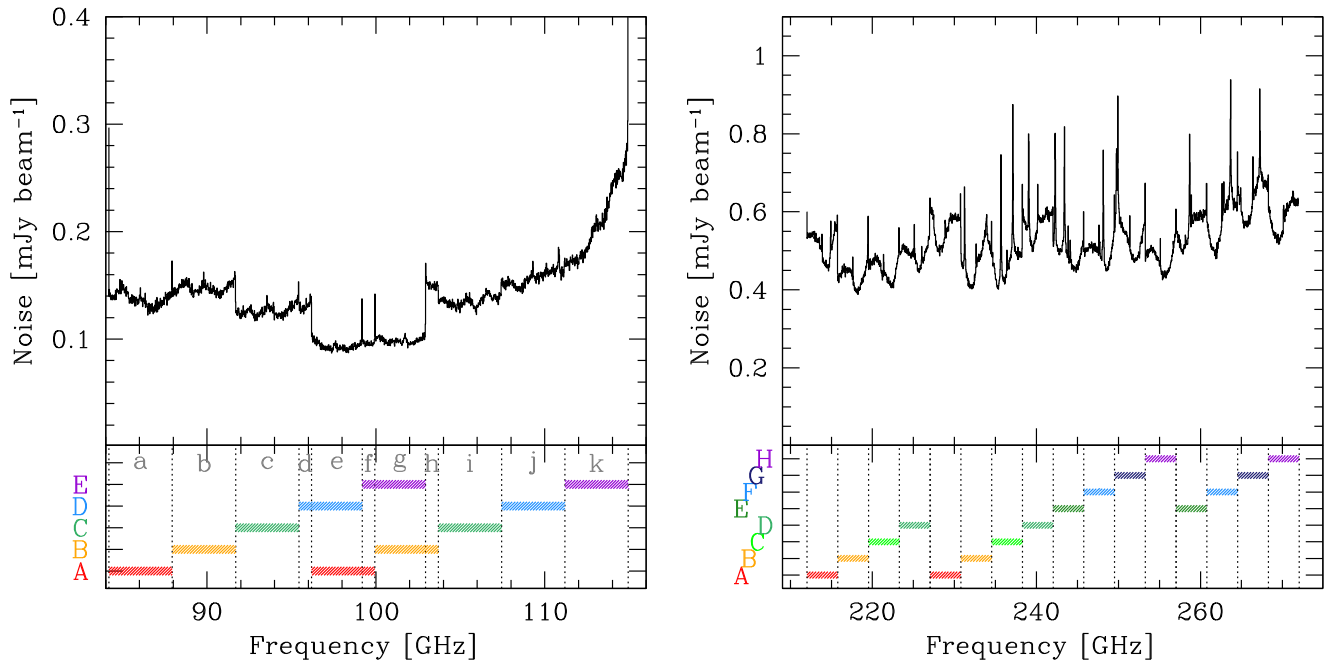
Figure 2. rms noise as a function of frequency in the 3 mm (left) and 1 mm (right) scans. At 3 mm, each channel is 19.5 MHz wide (five of the native channels), corresponding to 70 km s^{-1} at 84 GHz and 51 km s^{-1} at 115 GHz. The original frequency settings (A–H) are labeled in the bottom panel, together with the frequency blocks (a)–(k) used in the data reduction. At 1 mm, the channels are 31.3 MHz wide (four of the native channels), corresponding to 44 km s^{-1} at 212 GHz, and to 34 km s^{-1} at 272 GHz. To first order, we reach uniform sensitivity as a function of frequency in both bands. The increase in noise toward high frequencies (>113 GHz) in band 3 is due to the atmosphere (O_2).
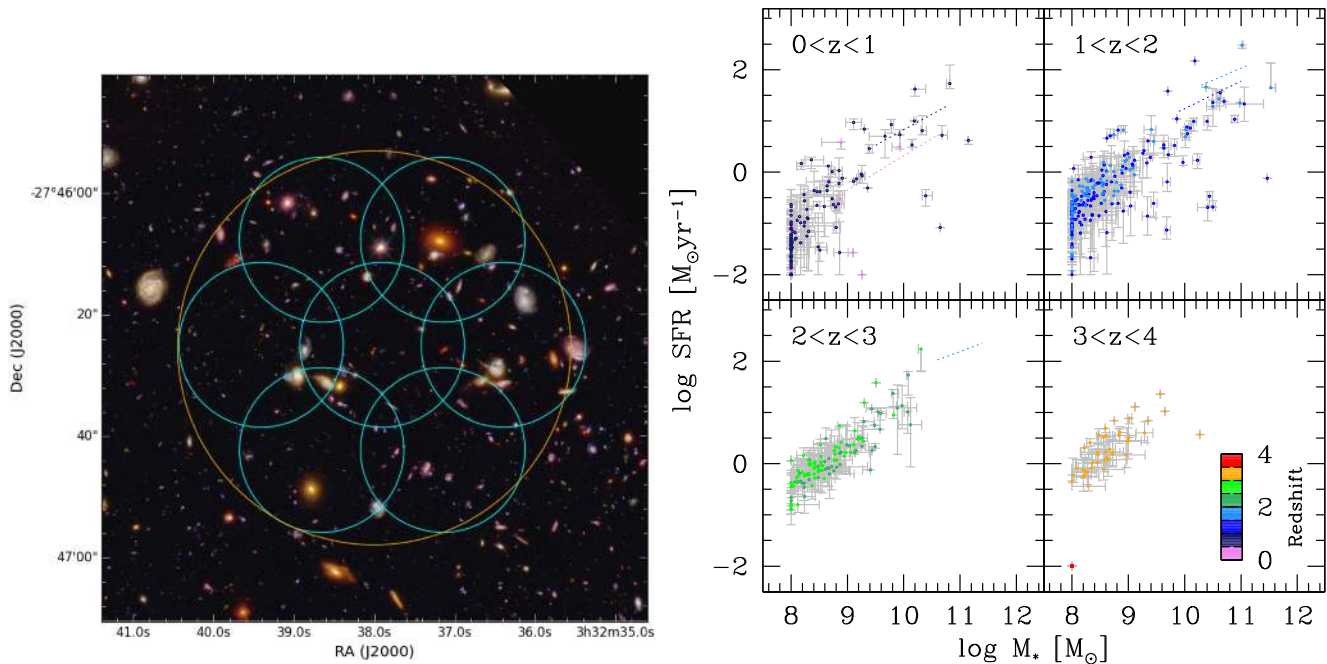
Figure 3. Left: the FWHM of the primary beam (i.e., areal coverage) of our 3 mm (orange) and 1 mm (cyan) observations, overlaid on a three-color *HST* F435W/F775W/F105W image of the field from the XDF survey (Illingworth et al. 2013). The circles show the primary beam of each pointing at the central frequencies of the two scans. Right: star-formation rates vs. stellar masses for the galaxies in the target field, derived from MAGPHYS fitting (described in Section 4). The four panels show galaxies in different redshift ranges.

Figures 1 and 2). The time allocated for both projects amounts to a total of ~40 hr including overheads (split approximately 50–50 between band 3 and band 6).

The 3 mm observations (ALMA Project ID: 2013.1.00146.S) were carried out between 2014 July 1st and 2015 January 6th. The 3 mm scan consisted of a single pointing

(R.A. = 03:32:37.90 decl. = −27:46:25.0, J2000.0) and five frequency settings (see Figure 2). Each setting had 4 × 1.875 GHz spectral windows (two in the upper side band and two in the lower side band), and was observed in three execution blocks. The native channel width is 3.9025 MHz, or ~12 km s^{-1} at ~100 GHz. Observations were

Table 2
Catalog of the Line Candidates Identified in Our Analysis

ID ASPECS... (1)	R.A. (J2000.0) (2)	decl. (J2000.0) (3)	Frequency (GHz) (4)	Flux (Jy km s⁻¹) (5)	FWHM (km s⁻¹) (6)	S/N (7)	Opt/NIR c.part? (8)	Comments (9)
3 mm (band 3)								
3 mm.1	03:32:38.52	−27:46:34.5	$97.567^{+0.003}_{-0.003}$	0.72 ± 0.03	500^{+30}_{-30}	19.91	Y	$J = 3$; $J = 7,8$ also detected
3 mm.2	03:32:39.81	−27:46:11.6	$90.443^{+0.003}_{-0.003}$	0.44 ± 0.08	540^{+30}_{-30}	12.80	Y	$J = 2$; $J = 5$ tentatively detected. Confirmed by opt. spectroscopy
3 mm.3	03:32:35.55	−27:46:25.7	$96.772^{+0.003}_{-0.003}$	0.13 ± 0.01	57^{+30}_{-30}	9.48	Y	$J = 2$ is ruled out by optical spectroscopy
3 mm.4	03:32:40.64	−27:46:02.5	$91.453^{+0.003}_{-0.003}$	0.23 ± 0.03	73^{+30}_{-30}	5.86	N	lack of counterpart suggests $J > 2$
3 mm.5	03:32:35.48	−27:46:26.5	$110.431^{+0.003}_{-0.003}$	0.18 ± 0.02	82^{+25}_{-25}	5.42	Y	$J = 2$ confirmed by optical spectroscopy
3 mm.6	03:32:35.64	−27:45:57.6	$99.265^{+0.003}_{-0.003}$	0.23 ± 0.02	160^{+30}_{-30}	5.40	N	lack of counterpart suggests $J > 2$
3 mm.7	03:32:39.26	−27:45:58.8	$100.699^{+0.003}_{-0.003}$	0.08 ± 0.01	60^{+25}_{-30}	5.40	N	lack of counterpart suggests $J > 2$
3 mm.8	03:32:40.68	−27:46:12.1	$101.130^{+0.003}_{-0.003}$	0.19 ± 0.01	100^{+25}_{-30}	5.30	N	no match with nearby galaxy; $J > 2$
3 mm.9	03:32:36.01	−27:46:47.9	$98.082^{+0.003}_{-0.003}$	0.09 ± 0.01	64^{+30}_{-30}	5.28	N	lack of counterpart suggests $J > 2$
3 mm.10	03:32:35.66	−27:45:56.8	$102.587^{+0.003}_{-0.003}$	0.24 ± 0.02	120^{+25}_{-25}	5.18	Y	$J = 3$ ($z = 2.37$) would match $z_{grism} = 2.33$
1 mm (band 6)								
1 mm.1	03:32:38.54	−27:46:34.5	$227.617^{+0.003}_{-0.003}$	0.79 ± 0.04	463^{+80}_{-10}	18.28	Y	$J = 7$
1 mm.2	03:32:38.54	−27:46:34.5	$260.027^{+0.003}_{-0.059}$	1.10 ± 0.05	478^{+11}_{-70}	16.46	Y	$J = 8$
1 mm.3	03:32:38.54	−27:46:31.3	$225.181^{+0.003}_{-0.003}$	0.22 ± 0.02	101^{+18}_{-18}	5.87	Y	$J = 3$ would imply $z = 0.54$, and $z_{grism} = 0.59$
1 mm.4	03:32:37.36	−27:46:10.0	$258.333^{+0.016}_{-0.003}$	0.27 ± 0.02	150^{+20}_{-20}	5.62	N	if [C II], tentative CO(6-5) detection is reported. Possibly lensed by foreground Elliptical?
1 mm.5	03:32:38.59	−27:46:55.0	$265.320^{+0.003}_{-0.031}$	0.72 ± 0.03	211^{+37}_{-10}	5.47	N	lack of other lines suggests $J = 4$
1 mm.6	03:32:36.58	−27:46:50.1	$222.553^{+0.003}_{-0.003}$	0.56 ± 0.02	302^{+12}_{-40}	5.45	Y	$J = 4$ yields $z = 1.07$, $J = 5$ yields $z = 1.59$, $J = 6$ yields $z = 2.11$, tentative second line for $J = 4$ or $J = 6$
1 mm.7	03:32:37.91	−27:46:57.0	$257.042^{+0.003}_{-0.003}$	1.78 ± 0.03	179^{+11}_{-11}	5.43	N	lack of other lines suggests $J = 4$
1 mm.8	03:32:37.68	−27:46:52.6	$222.224^{+0.022}_{-0.003}$	0.39 ± 0.02	210^{+30}_{-12}	5.33	N	lack of counterpart excludes $J = 2,3$; lack of second line exclude CO. [C II]?
1 mm.9	03:32:36.14	−27:46:37.0	$249.085^{+0.016}_{-0.003}$	0.34 ± 0.02	150^{+20}_{-20}	5.19	N	$J = 4$; lack of counterparts excludes J<4, and lack of other lines excludes J>4
1 mm.10	03:32:37.08	−27:46:19.9	$237.133^{+0.003}_{-0.003}$	0.49 ± 0.04	281^{+48}_{-12}	5.18	N	$J = 4$ or 6 due to lack of counterparts and other lines. $J = 4$ favored because of excitation
1 mm.11	03:32:37.71	−27:46:41.0	$223.067^{+0.003}_{-0.025}$	0.27 ± 0.02	169^{+35}_{-12}	5.16	N	lack of other lines suggests $J = 3$

Note. (1) Line ID. (2–3) R.A. and decl. (J2000). (4) Central frequency and uncertainty, based on Gaussian fit. (5) Velocity integrated flux and uncertainty. (6) Line full width at half maximum, as derived from a Gaussian fit. (7) Signal-to-noise as measured by the line searching algorithm. (8) Spatially coincident optical/NIR counterpart? (9) Comments on line identification.

carried out in a relatively compact (C34-2) array configuration with 29–41 antennas, with baselines ranging between 12 and 612 m. The quasar J0348–2749 was observed in the majority of the execution blocks as phase and amplitude calibrator, while Uranus and the quasars J0334–4010 and J0334–4008 were used as flux and bandpass calibrators. Data were calibrated and imaged with the *Common Astronomy Software Applications* package (CASA) version 4.2.2 of the ALMA pipeline.

To combine the different setups, we adopted the following approach. (1) For each execution block, we split out cubes in frequency ranges as shown in Figure 2 (a)–(k). (2) The frequency ranges marked with the letters (e)–(g), i.e., where upper and lower side band observations from different frequency settings overlap, were re-sampled using the CASA task ms.cvel. (3) We then combined all the available data for each individual frequency range (a)–(k) using the CASA task concat. (4) Upper and lower side band data come with different weighting scales, though the data quality is comparable. We therefore ran statwt in order to homogenize the

weighting system in the concatenated data. (5) We combined all the frequency ranges using the task concat again.

We imaged the 3 mm cube after averaging over two and five native channels (7.8 MHz and 19.5 MHz respectively) using natural weighting. The 19.5 MHz channels correspond to 70 km s⁻¹ at 84 GHz, and 51 km s⁻¹ at 115 GHz. We created a band 3 continuum map as well (see discussion in Section 3.4). The corresponding primary beams of the ALMA antennas are 75″ at 84 GHz and 55″ at 115 GHz. The restored synthesized beam size is 3″.5 × 2″.0 (FWHM) with PA = 84° . We thus adopted a pixel scale of 0″.5 pixel⁻¹, and an image size of 90″ × 90″. A primary-beam correction has been applied for all quantitative analyses. The final data set covers the frequency range of 84.176–114.928 GHz, and reaches an rms of 0.1–0.25 mJy beam⁻¹ per 19.5 MHz channel (see Figure 2). For comparison, the PdBI spectral scan at 3 mm in the *Hubble* Deep Field North (Decarli et al. 2014, Walter et al. 2012, 2014) reached a sensitivity of ~0.3 mJy beam⁻¹ per 90 km s⁻¹ channel, or ~0.4 mJy beam⁻¹ at the sampling adopted here. Therefore, these ALMA observations are a factor of three to

four deeper at $\nu < 113$ GHz than the previous 100 hr (on-source) effort with PdBI (Decarli et al. 2014).

The 1 mm observations (ALMA Project ID: 2013.1.00718.S) were carried out between 2014 December 12th and 2015 April 21st. In order to cover a similar area as the 3 mm pointing, a seven-point mosaic was observed, centered on the same coordinates as for the 3 mm observations (see Figure 3). For each pointing position, eight frequency settings were needed to cover the entire band (see Figure 2), resulting in continuous coverage from 212 to 272 GHz. In this case, there was no overlap between different spectral windows of various frequency tunings (see Figure 2). Observations were carried out in the most compact available array configuration (C34-1) with 30–34 antennas. Baselines ranged between 12 and 350 kλ. The quasar J0348–2749 was adopted as a phase and amplitude calibrator, while Uranus and the quasar J0334–4008 acted as flux and bandpass calibrators. The cube was imaged in spectral samplings of 4, 8, and 12 native channels, corresponding to 15.6 MHz, 31.2 MHz, and 46.8 MHz, respectively, as well as in a continuum image. The 31.2 MHz sampling corresponds to 44 km s^{-1} at 212 GHz and to 34 km s^{-1} at 272 GHz. We adopted natural weighting, yielding a synthesized beam of $1\farcs5 \times 1\farcs0$ with PA $= -79°$. We adopted a pixel scale of $0\farcs3$ per pixel. The final mosaic covers a region of approximately $75'' \times 70''$ to the half-sensitivity point.

3. LINE SEARCH

The data reduction resulted in two data cubes, one in band 3 and one in band 6, as well as continuum maps, which we discuss later (Section 3.4). We here describe our methodology to search for line emitting sources in these cubes.

3.1. The Blind Line Search

For our blind search of line candidates, we developed an IRAF-based routine, findclumps, which operates directly on the imaged data cubes. The script performs floating averages of a number of channels, computes the rms of the averaged maps, and searches for peaks exceeding a certain S/N threshold using the IRAF task daofind. The position, frequency, and S/N of the recovered candidates is saved. As input, we used the 7.8 MHz and 31.2 MHz sampling for the 3 mm and 1 mm cubes respectively. Since the significance of a line detection is maximized when averaging over a frequency range comparable to the actual width of the line, we ran our search over 3-, 5-, 7-, and 9-channel windows, i.e., kernel line widths of $\sim$50–300 km s^{-1} (an inspection using larger line-widths did not result in additional detections—this is also supported by our completeness test, see below).

The list of line candidates identified by this procedure is then trimmed in order to keep only candidates that lie within $\sqrt{2} \times$ the primary-beam radius at 3 mm ($= 53''$ at 84 GHz, 39$''$ at 115 GHz), equivalent to a response of $\sim$30% and within a fixed radius of $30\farcs9$ at 1 mm (given that the latter is a mosaic).

The floating-average approach and the use of different windows of spectral sampling allow us to avoid missing candidates because of a priori choices in terms of spectral bins. However, our candidate lists are subject to multiplicity both spatially and spectrally. Moreover, the 1 mm search is bound to pick up bright continuum sources as potential line candidates. We therefore masked a posteriori the line candidates associated with the two brightest 1 mm continuum sources (see Section 3.4

and Paper II). We consider as duplicates line candidates that are offset by less than one synthesized beam ($\sim2\farcs5$ at 3 mm, $\sim1\farcs5$ at 1 mm) and that appear in consecutive channels in the floating average.

When assessing the reliability of our line candidates, we need to keep two separate issues in mind ("fidelity" and "completeness," which we discuss in Sections 3.1.1 and 3.1.2).

3.1.1. Fidelity

First, is a given line detection significant? This question is harder to address in practice than one would naively think: the S/N of a single detection will be a function of the width of the line, and the noise in the cubes is not Gaussian. The best way to address this question is to perform two independent searches: (1) for positive emission—these candidates would correspond to both real astrophysical sources and noise peaks—and (2) for negative emission—these candidates would only correspond to non-astrophysical sources.[38] These latter sources can be used to define a term that we refer to as fidelity, i.e., we can statistically subtract the unphysical "negative" lines from the physical "positive" ones.

We thus assess the degree of fidelity in our line search by running the same search over the positive and negative peaks. The basic assumption is that, given the interferometric nature of our data set, and that we do not expect to detect absorption features against very high-S/N continuum emission, all the "negative" line candidates will be noise peaks, while the "positive" line candidates will be a mixture of noise peaks and genuine lines. The search for negative peaks is performed in the exact same way as the one for positive emission. By comparing the results of these two searches, we can quantify the fidelity of our search at a given line candidate significance as follows.

$$\text{fidelity}(\text{S/N}) = 1 - \frac{N_{\text{neg}}(S/N)}{N_{\text{pos}}(S/N)} \qquad (1)$$

where $N_{\text{pos}}(S/N)$ and $N_{\text{neg}}(S/N)$ are the number of positive and negative line candidates with a given S/N, respectively. This definition is such that, if the number of negative candidates at a given S/N is comparable to the number of positive candidates, then the fidelity is null; if it is negligible, then the fidelity is close to 100%. For the analysis of our blind search, we request a fidelity level of 60% or higher. This threshold was chosen so that at the lowest accepted significance, more than half of the "positive" line candidates are real. We determine the signal-to-noise ratio (S/N) computed by findclumps as follows. For each floating-averaged channel, we compute the map rms (which will constitute the "noise" term) and we take the peak pixel value at the position of a line candidate as "signal." We emphasize that, since the averaging window is not optimized to match the actual width of a line candidate (also this approach assumes spatially unresolved line emission), this definition of S/N is by construction conservative. The S/N values of each line candidate are reported in Table 2. In Figure 4, we show how the fidelity of our line search changes as a function of the

---

[38] An interesting hypothesis is that at least some of the negative sources are in fact real absorption systems due to absorption against the CMB. However, our checks revealed that none of the significant negative sources are either associated with a galaxy visible in the UDF, nor with a strong continuum emission. We conclude that the negative sources revealed by our search are physically implausible.
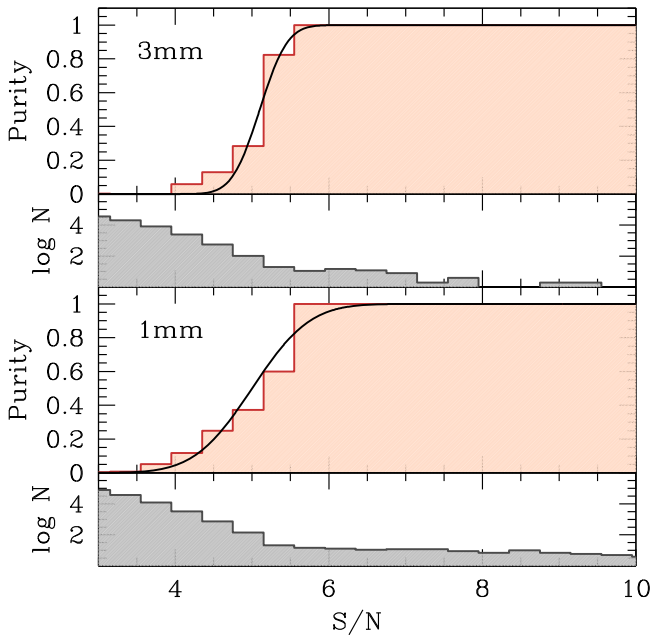
Figure 4. Fidelity in our line search, plotted as a red histogram as a function of the line S/N of the individually detected candidates. The fidelity is defined as in Equation (1). The number of candidates as a function of S/N is also shown. We model the fidelity dependence on S/N as an error function (solid black line). The search reaches 60% fidelity at S/N ~ 5.2 both at 1 mm and 3 mm; though, the latter shows a sharper increase of fidelity with S/N. We choose a fidelity level of >60% for the sources that enter our analysis, implying that, at the lowest significance, out of a sample of 10 candidates, 6 are likely real, and 4 sources at similar S/N were also detected with negative signal.

line S/N. It is convenient to have an analytical description of the fidelity dependence on S/N. While not physically motivated, the following error function provides a good description of the observed trend, with the following parameterization.

$$\text{fidelity}(\text{S/N}) = \frac{1}{2}\, \text{erf}\!\left(\frac{\text{S/N} - C}{\sigma}\right) + 0.5 \qquad (2)$$

where $C_{3mm} = 5.1$, $C_{1mm} = 5.0$, $\sigma_{3mm} = 0.4$, $\sigma_{1mm} = 0.8$. This implies that we reach 60, 80, and 95% fidelity levels at S/N = 5.17, 5.34, and 5.57 at 3 mm, and at S/N = 5.15, 5.50, and 5.97 at 1 mm. We will use this equation to assess the fidelity for our individual line detections.

3.1.2. Completeness

The second question concerns our ability to extract faint sources from our data cubes (completeness). We address this by inserting artificial line sources of various strengths and widths in our data cubes, then calculating our ability to recover them in our line search. This is a standard way of deriving the completeness of sources in the low S/N regime.

We assess the level of completeness in our blind line search by adding 2500 artificial line sources to the data cube, re-running our line searching algorithm, and comparing the number of recovered sources with the input catalog. The line candidates are assumed to have a Gaussian profile along the spectral axis, and the shape of the synthetic beam in the maps. The line spatial positions, peak frequencies, peak flux densities and widths are randomly generated with uniform distributions as follows: R.A., decl., and the line peak frequency are required

to be homogeneously distributed within the cubes. The line peak flux density range between 0.22 and 1.00 mJy (at 3 mm) and between 0.5 and 2.0 mJy (at 1 mm), where the fainter side is set to roughly match the 1σ typical limit of each channel. The line widths span the range of 50–500 km s^{-1}. In Figure 5, we show how the completeness of our line search is a function of the input width and peak flux density of the lines. At 3 mm, the completeness is >50% for peak flux densities $F_\nu^{\text{line}} > 0.45$ mJy, and for line widths $\Delta v > 100$ km s^{-1}. We also observe a minor dependence of the completeness on the frequency due to the decreasing sensitivity toward the high-frequency end of the scan (see Figure 2). The line search in the 1 mm mosaic shows a completeness >50% for peak flux densities >0.8 mJy and widths >100 km s^{-1}. These completeness corrections will be used extensively in Paper III.

3.2. Line Candidates

3.2.1. Properties

For our subsequent analysis, we consider only those sources that have a fidelity of greater than 60% and where the extracted line is detected at $>2\sigma$ in consecutive channels (width: ~25 km s^{-1} at 3 mm, ~40 km s^{-1} at 1 mm). Our blind search resulted in 10 line candidates from the 3 mm search, and 11 line candidates from the 1 mm search (see Table 2 and the figures in the Appendix). Given our requirement on the fidelity in our search, we expect that <4 out of these line candidates are spurious in each band. We show the candidates, sorted by S/N of the line emission, in Figures 8 (band 3) and 9 (band 6). In each case, the left panel shows an *HST* color composite, and the middle panel shows the *HST* image in grayscale, and the CO line candidates in contours. The right panel shows the spectrum extracted at the position of the line candidate. The basic parameters of the candidate lines (R.A., decl., frequency, integrated flux, line width, and S/N) are summarized in Table 2.

3.2.2. Optical/NIR Counterparts

We have searched for optical/NIR counterparts by matching the positions of the sources in the multi-wavelength catalogs (Section 2.2) with our line candidates. Whether a specific CO line candidate has a counterpart or not is summarized in column 8 of Table 2 (see also Figures 8 and 9). The lines that show an optical/NIR counterpart with matching redshift are discussed in detail in Paper IV.

3.2.3. Redshift Determination

Given the (almost) equi-distant spacing of the rotational transitions of CO, it is not straightforward to assign a unique redshift to each candidate in a number of cases.

Multiple CO lines? For certain redshifts, more than one CO transition is covered by our band 3 and band 6 scans. We use this information to constrain the redshift of some of the candidate. Likewise, in other cases a certain redshift solution can be ruled out if other detectable lines are not detected. This information is given in the "comments" column of Table 2.

Optical/NIR spectroscopic redshifts. In some cases, spectroscopic redshifts are available for the optical/NIR counterparts, either through long-slit spectroscopy (Le Fèvre et al. 2005; Kurk et al. 2013; Skelton et al. 2014; Morris et al. 2015), or *HST* grism observations (Morris et al. 2015; Momcheva
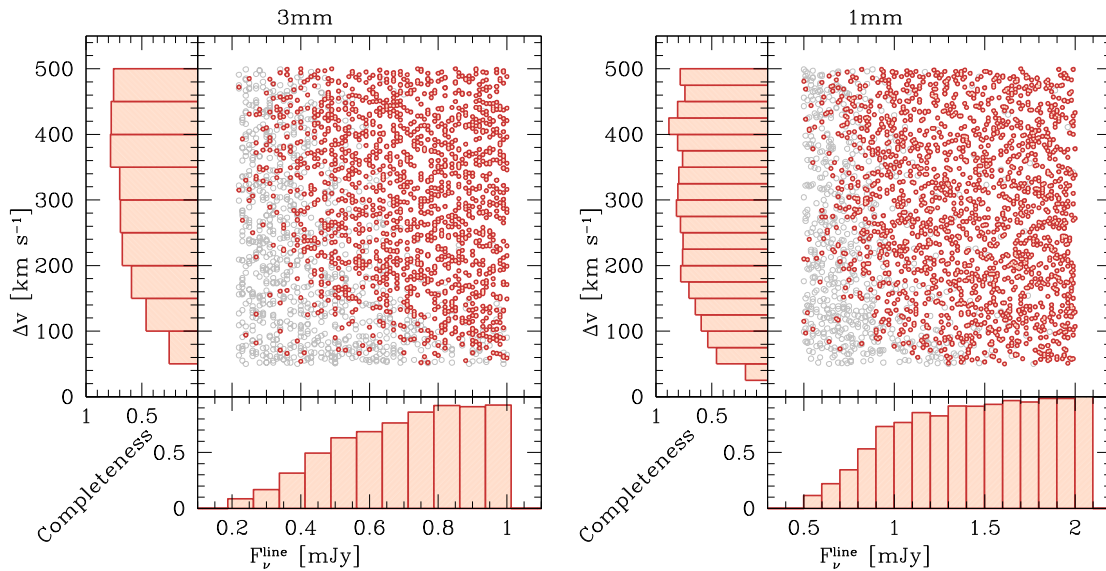
Figure 5. Completeness assessment of our line search. In each diagram, each circle represents an artificially injected line candidate. Filled symbols highlight the candidates that we recover in our analysis. The histograms show the marginalization along the y- and x-axes respectively, showing the level of completeness (i.e., the fraction of input line candidates that our script successfully identifies) as a function of the line width (Δv) and peak flux density (F_ν^{line}), respectively. The 3 mm case is shown on the left, the 1 mm one is on the right.

et al. 2016). We also record this information in the "comments" column of Table 2.

Lack of optical/NIR counterparts. In a number of cases, no optical/NIR counterpart of the line candidate is visible in the *HST* image. This can be due to the fact that the source is spurious. However, if the candidate was real, and assuming that there is no signficant reddening by dust, then the exquisite depth of the available optical/NIR observations (in particular, the *HST*/WFC3 IR images and the Spitzer/IRAC images) can place constraints on the stellar mass of galaxies as a function of redshift. Our MAGPHYS fits (see Section 4) of the available photometry suggest that a galaxy securely detected in the H-band (1.6 μm) at >50 nJy (corresponding to a secure, >10σ detection in a few bands) has a stellar mass of >4 × 10^6 $M_\odot$, >2 × 10^7 $M_\odot$, and >10^8 $M_\odot$ at $z = 0.5$, 1.0, and 2.0, respectively. Because of the combination of low molecular gas content, and likely elevated α_{CO} values (Bolatto et al. 2013), we do not expect to detect CO in galaxies with $M_* \ll 10^9$ $M_\odot$. Therefore, we can use the lack of an optical counterpart to set constraints on the redshift of the candidate. In particular, we assume that line candidates selected in band 3 and lacking an optical/NIR counterpart are at $z > 2$ (i.e., the line is identified as CO(3–2) or a higher-*J* transition). In the case of band 6 candidates, we give priority to the constraints from the multiple line (non-)detection. The "lack of counterpart" argument is chosen only to rule out the lowest-z scenarios (J<4, corresponding to $z < 0.695$). This additional constraint on the line candidates is also given in the "comments" column of Table 2.

The total CO flux of all line candidates is 2.55 Jy km s^{-1}, whereas the total flux of the candidates that have no optical/NIR counterpart is 0.83 Jy km s^{-1} (from Table 2), i.e., ~33% of the total. Because some of the line candidates that do not show an optical/IR counterpart are likely spurious, and considering that the brightest CO detections with optical/NIR counterparts dominate the total emission, the flux fraction of

real objects without an optical/NIR counterpart is likely lower.

3.3. Other CO- and [C II]-detected Galaxies

This paper describes our blind search results. An alternative approach to finding line emission in the galaxies covered by our observations is to search the cubes at the position of optical galaxies that have accurate spectroscopic redshifts. Such additional information (position and redshift) could, in principle, help to identify plausible CO or [C II] emission lines at lower significance than those revealed by the automatic search. We have performed such a search, which has resulted in the detection of three additional galaxies that are tentatively detected in CO emission. These detections are presented and discussed in Paper IV. We note that the inclusion of these three galaxies would not change the statistical analysis based on the much larger sample presented here. Similarly, in Paper V, we investigate the presence of [C II] emission in galaxies for which a photometric redshift from SED fitting or the detection of a clear drop-out in the z band suggests redshifts $z > 6$.

3.4. Continuum Emission

The frequency scans can be used to obtain very-high-sensitivity maps of the continuum, by collapsing the two data cubes along the frequency axis, after removing the few channels that contain significant line emission. The resulting continuum maps with noise levels at their center of 3.8 μJy beam^{-1} (band 3) and 12.7 μJy beam^{-1} (band 6) are shown in Figure 6 and will be discussed in detail in Paper II.

4. COMPARISON WITH EXPECTATIONS

We present a detailed comparison of the evolution of the CO luminosity functions, and the resulting cosmic density of molecular hydrogen in Paper III. As a sanity check, we here
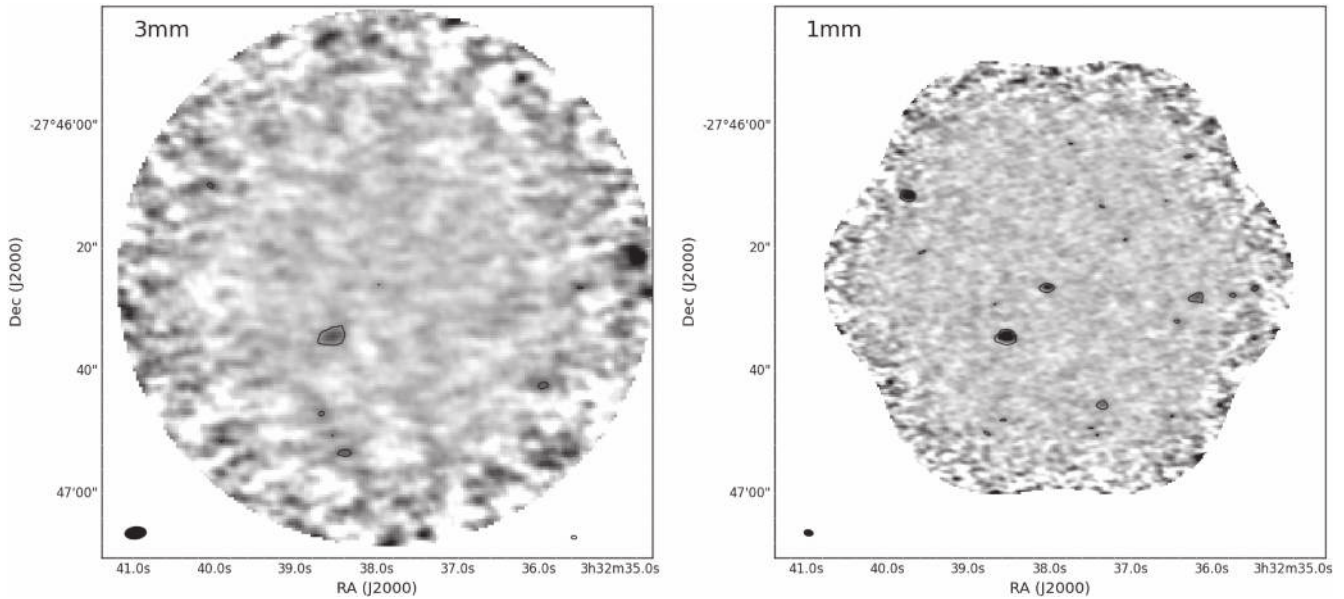
Figure 6. Continuum images at 3 mm (left) and 1 mm (right). In both panels, we plot a contour at the 3σ level, where 1σ is 3.8 μJy beam^{-1} in the 3 mm observations and 12.7 μJy beam^{-1} in the 1 mm observations. Both images have been primary-beam corrected. Note that at 3 mm, only one source is clearly detected at S/N > 3. The 1 mm continuum map is extensively discussed in Paper II.
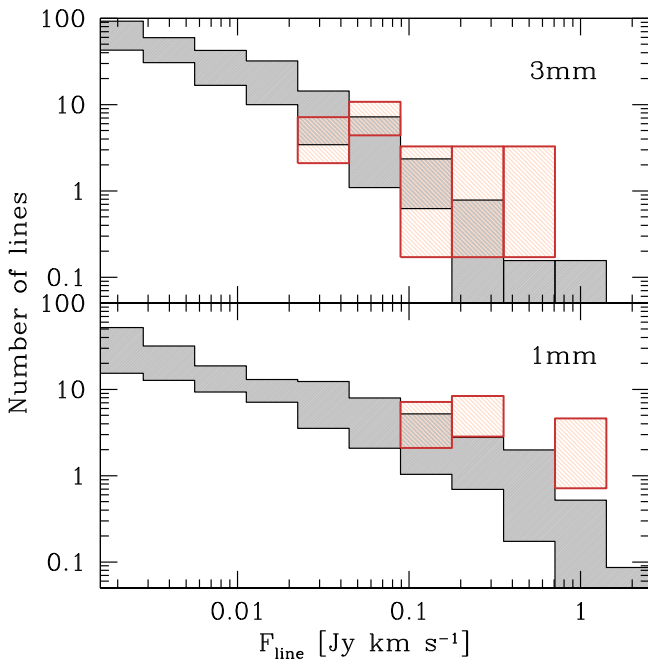

Figure 7. Comparison between the MAGPHYS-based predictions of line fluxes from da Cunha et al. (2013b), in gray, and the flux distribution of the line candidates actually observed in our survey (red boxes). The numbers from da Cunha et al. (2013b) are computed over the whole UDF, and scaled down to match the same area coverage of our survey. We consider here only the transitions that we cover in our scan (see Table 1). The lower and upper sides of the shaded gray area refer to the cases of Milky-Way- and M82-like CO excitation. In the case of our ALMA constraints, the vertical size of the boxes shows the Poissonian uncertainties in the number of lines detected in a certain flux range. Our ALMA constraints are not corrected for the fidelity and completeness of our line search. The number of detected lines is in general agreement with the expectations, in particular, if one keeps in mind that ASPECS 1 mm.1/2, whose high-J CO emission dominates the highest flux bin at 1 mm, was not included in the da Cunha et al. (2013b) study.

briefly compare the number of CO-detected galaxies with previous expectations based on a multi-wavelength analysis of the galaxies in the UDF.

For each galaxy in the UDF, da Cunha et al. (2013b) estimated stellar masses, SFRs, IR luminosities, and expected CO and [C II] fluxes and luminosities by fitting the optical/NIR photometry provided by Coe et al. (2006), using the MAGPHYS spectral energy fitting code (da Cunha et al. 2008, 2015). We show the resulting star-formation rates, and stellar masses, in four redshift bins in the right-hand panel of Figure 3. Note that typical selections of main-sequence galaxies for CO follow-up usually target stellar masses of $M_{star} > 10^{10}$ $M_{\odot}$ and star-formation rates SFR > 50 $M_{\odot}$ yr^{-1} (e.g., Daddi et al. 2008, 2015; Genzel et al. 2008, 2015; Tacconi et al. 2008, 2010). Specifically, this selection would target galaxies in the top-right part of each diagram because the UDF contains many galaxies that are much less massive/star forming.

In Figure 7, we show the expected numbers of line detections in the 3 mm and 1 mm bands, respectively. In this plot, the expected number of lines from da Cunha et al. (2013b), originally computed for the entire $3' \times 3'$ UDF, has been scaled to the areal coverage of our survey. In da Cunha et al. (2013b), two extreme CO excitation cases were considered in order to transform predicated CO(1–0) luminosities into higher-J line luminosities: the low-excitation case of the global Milky-Way disk, and the high-excitation case of the nucleus of the local starburst galaxy M82 (Weiß et al. 2007). For each line flux plotted on the abscissa, this range of excitation conditions is indicated by the gray region on the ordinate.

In this figure, we compare to our observations, which are plotted as red-shaded regions. For each flux bin on the abscissa, the number counts with the Poissonian error bars are shown on the ordinate. For this back-of-the-envelope calculation, we do not correct our measurements for completeness or fidelity (this is done in detail in Paper III). A number of things need to be kept in mind in this comparison: the total number of detected sources is low, which results in large uncertainties in the measurements on the ordinate. At 1 mm, the data in the highest flux bin (around 1 mJy km s^{-1}) is significantly higher than the
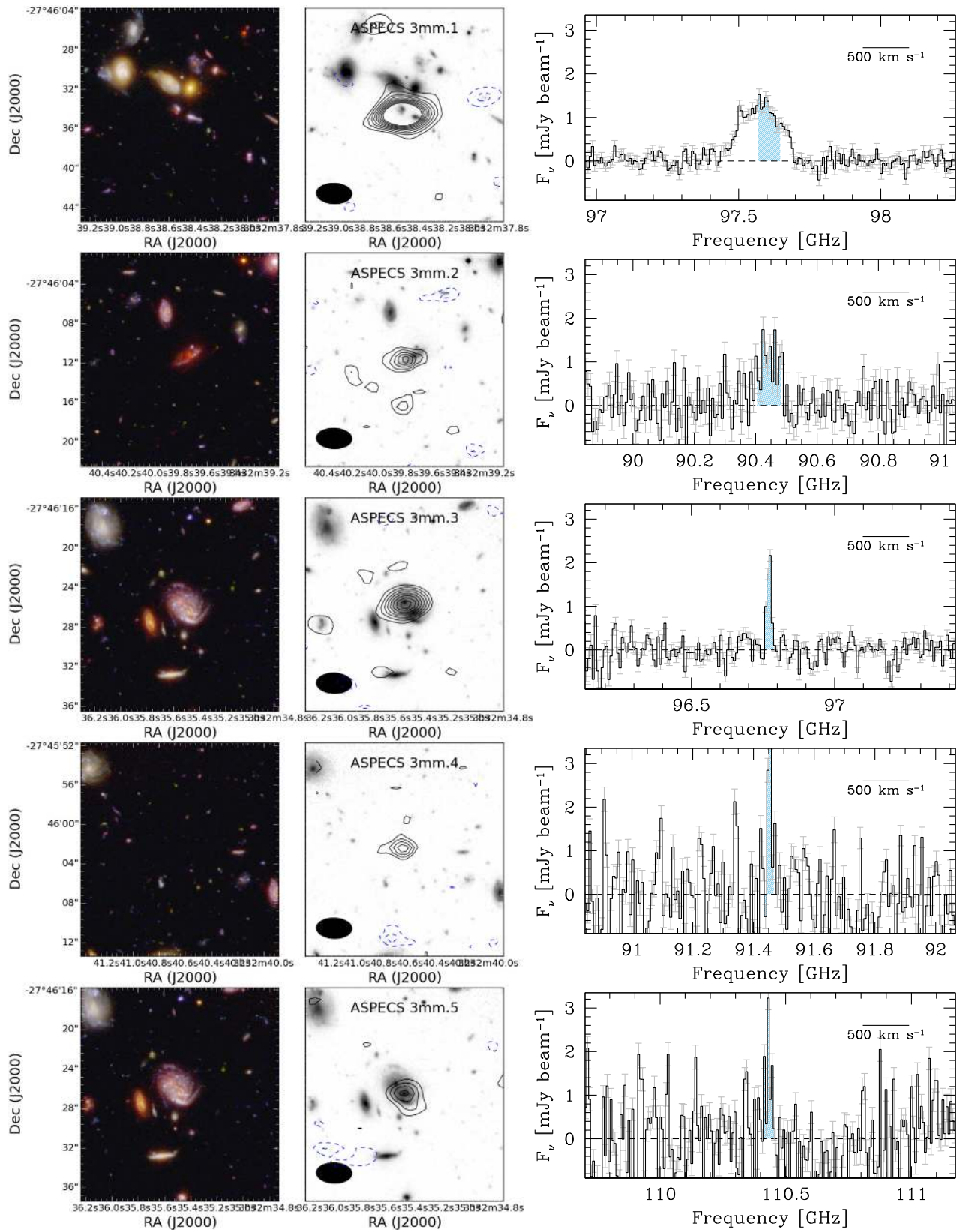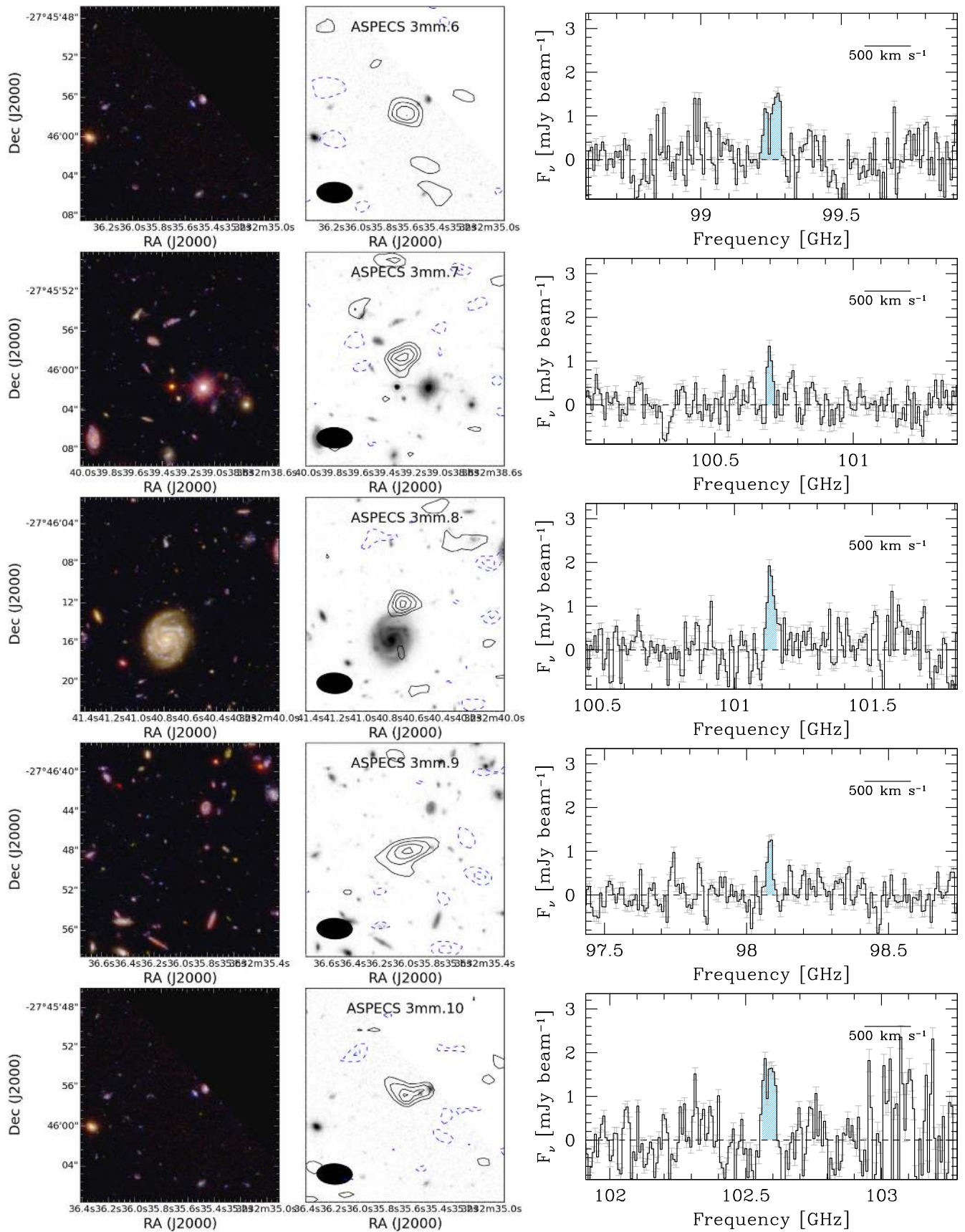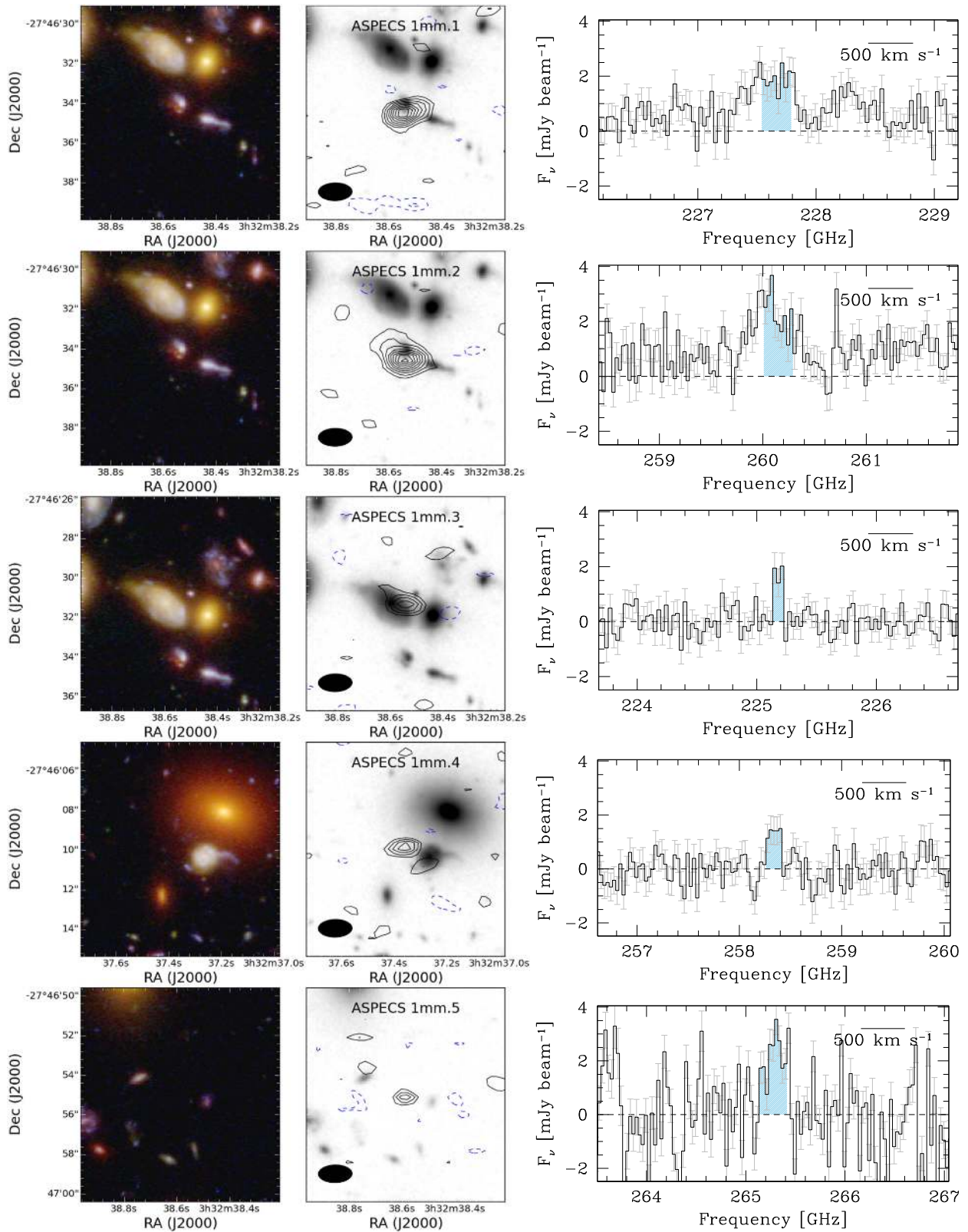
Figure 8. Left: optical/NIR *HST* multi-color image centered on the line candidates discovered in the blind search at 3 mm (using the F125W, F775W, and F435W filters; Illingworth et al. 2013). Middle: CO contours of the candidate line maps resulting from our line search described in Section 3. Positive (negative) contours of the CO emission are plotted in solid black (dashed blue), where the contours mark the ±2, 3, 4, ... -σ isophotes (σ is derived from the respective line map). Each postage stamp is 20″ × 20″ and the size of the synthesized beam is show in the lower left. Right: spectrum of the line candidate. The blue shading marks the channels that the line-searching algorithm used to compute the line S/N (this is why the shading does not cover the entire width of the brightest source). All line parameters are summarized in Table 2.

Figure 8. (Continued.)

Figure 9. Left: optical/NIR *HST* multi-color image centered on the line candidates discovered in the blind search at 1 mm (using the F125W, F775W, and F435W filters; Illingworth et al. 2013). Middle: contours of the candidate line maps resulting from our line search described in Section 3. Positive (negative) contours are plotted in solid black (dashed blue), where the contours mark the $\pm 2, 3, 4, \ldots -\sigma$ isophotes (σ is derived from the respective line map). Each postage stamp is $20'' \times 20''$ and the size of the synthesized beam is show in the lower left. Right: spectrum of the line candidate. The blue shading marks the channels that the line-searching algorithm used to compute the line S/N. All line parameters are summarized in Table 2.
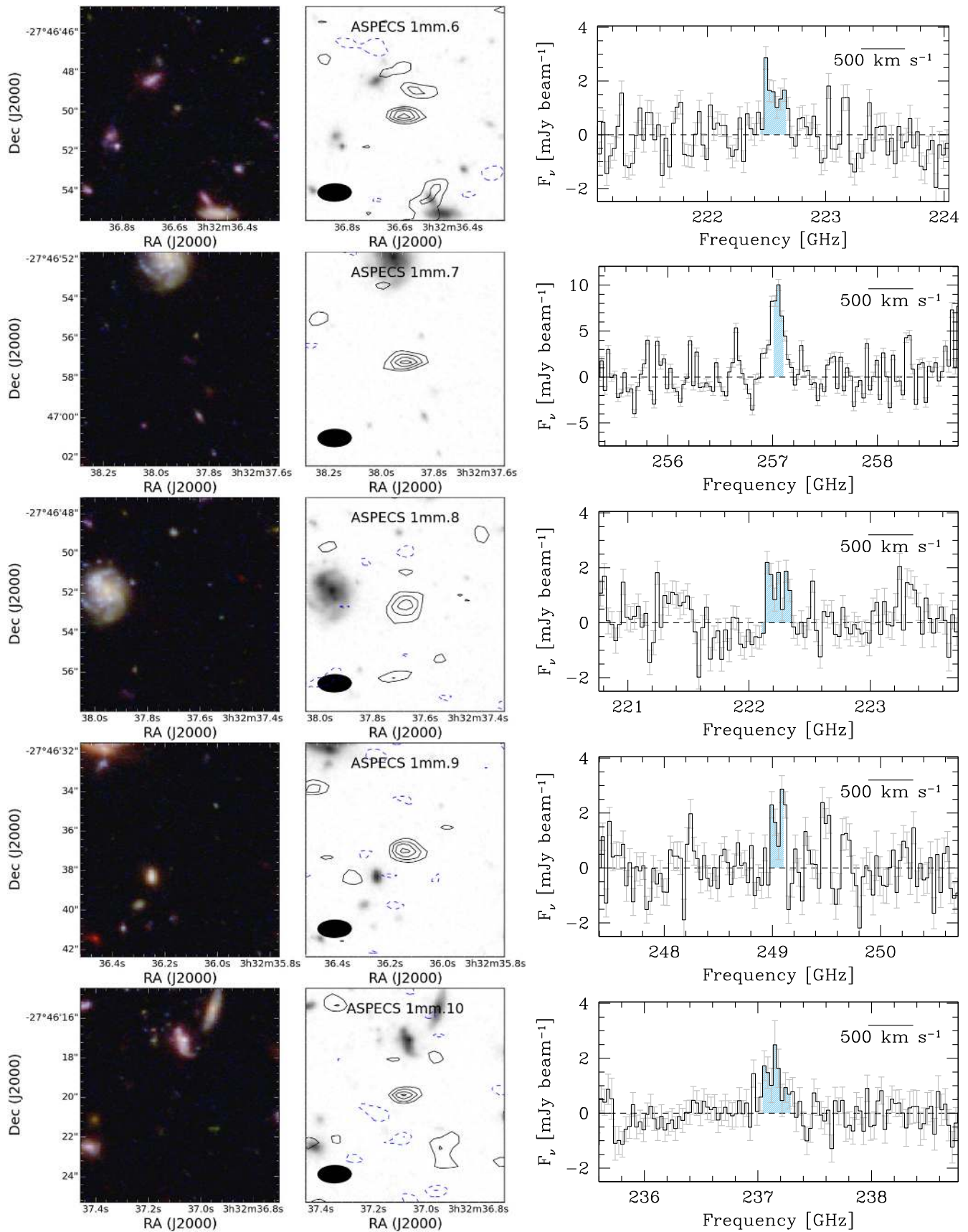
Figure 9. (Continued.)

Figure 9. (Continued.)

5. SUMMARY
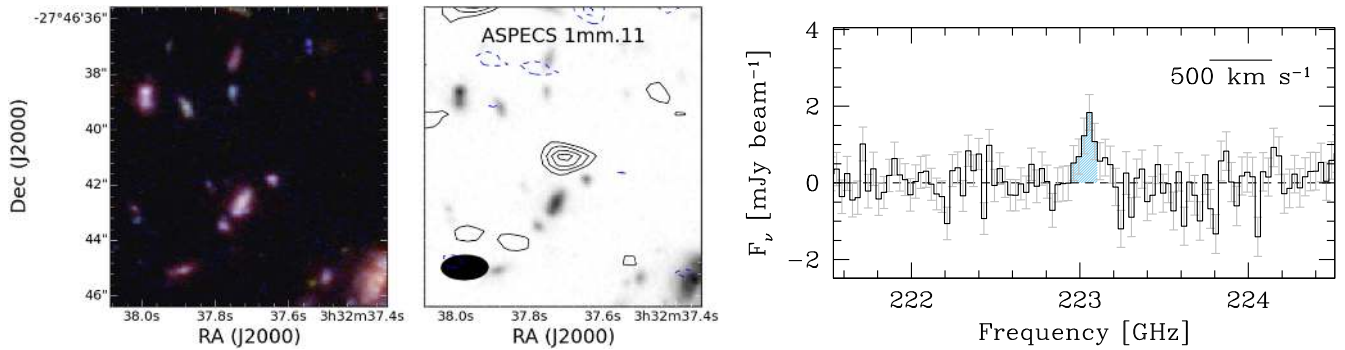
predictions. Note, however, that the measurement includes the two high-*J* CO detections of ASPECS 1 mm.1/2, a galaxy that was not included in the UDF catalog on which the predictions by da Cunha et al. (2013b) were based. Larger areas are required to see if there is indeed an excess of high-*J* CO emission present. Overall, we conclude that within the large uncertainties, there is reasonable agreement between the observations and previous expectations. This is discussed in detail in Paper III.

5. SUMMARY

We present the rationale for and the observational description of ASPECS, our complete band 3 and band 6 spectral line scan with ALMA of the *Hubble* UDF. This field was chosen because it has the deepest multi-wavelength data available, it will remain a key cosmological deep field in the future (in particular, in the era of *JWST*) and is easily observable by ALMA. We discuss our survey design of the full frequency scans in band 3 (84–115 GHz) and band 6 (212–272 GHz) and report the relevant parameters of our final data set. Critically, ALMA allows us to reach approximately uniform depth (line sensitivity: $\sim L'_{CO} \sim 2 \times 10^9$ K km s^{-1} pc^2) across a broad range of redshifts.

The spectral line scans cover the different rotational transitions of the CO molecule at different redshifts, leading to essentially full redshift coverage. We present a customized algorithm to identify line candidates in our data. This algorithm takes varying line widths of the possible emission lines into account. We assess the fidelity of our line search by comparing the number of positive candidates to the respective number of negative candidates, the latter being unphysical. We also calculate the completeness of our search, by quantifying our ability to recover artificial sources in our data. We present CO spectra and *HST* postage stamps of the most signficant detections. Based on whether multiple CO lines are detected, and whether optical spectroscopic (either slit or grism) redshifts as well as optical/NIR counterparts exist, we give constraints on the most likely line identification of our candidates.

Out of the 10 line candidates (3 mm band) reported in our search (Table 2), we expect <4 candidates to be spurious, given our statistical analysis. There are a number of line candidates at positions where no optical/NIR counterpart is present. The total CO flux of these candidates is less than 33% of the total flux of all candidates, i.e., candidate sources without counterparts only contribute a small fraction of the total measured flux in the targeted field. We also present continuum maps of both the band 3 and band 6 observations. The

observed flux distribution of the line candidates is in general agreement with the empirical expectations by da Cunha et al. (2013b) based on SED modeling of the optical/NIR emission of galaxies in the UDF.

The data presented in this paper (Paper I) form the basis of a number of dedicated studies presented in subsequent papers.

1. In Paper II (Aravena et al. 2016a), we present 1.2 mm continuum number counts, dust properties of individual galaxies, and demonstrate that our observations recover the cosmic infrared background at the wavelengths considered.
2. In Paper III (Decarli et al. 2016a), we discuss the implications for CO luminosity functions and the resulting constraints on the gas density history of the universe. Based on our data, we show that there is a sharp decrease (by a factor of approximately five) in the cosmic molecular gas density from redshifts of ~3 to 0.
3. In Paper IV (Decarli et al. 2016b), we examine the properties of those galaxies in the UDF that show bright CO emission and discuss these also in the context of the bright optical galaxies that are not detected in CO.
4. In Paper V (Aravena et al. 2016b), we search for [C II] emitters in previously reported Lyman-break galaxies at $6 < z < 8$.
5. In Paper VI (Bouwens et al. 2016), we investigate where high-redshift galaxies from ASPECS lie in relation to known IRX-β and IRX-stellar mass relationships, concluding that less dust continuum emission is detected in $z > 2.5$ than expected (unless high dust temperatures, $T \sim 50$ K, are assumed).
6. Finally, in Paper VII (Carilli et al. 2016), we discuss implications on CO intensity mapping experiments, and contributions toward the emission from the cosmic microwave background.

The data presented here demonstrate the unique power of ALMA spectral scans in well-studied cosmological deep fields. The current size of the survey is admittedly small, limited by the amount of time available in ALMA "early science." More substantial spectral scan surveys with ALMA of the full UDF (and beyond) will become feasible once ALMA is fully operational.

APPENDIX
LINE CANDIDATES FROM THE BLIND SEARCH

In this appendix, we show postage stamps and extracted spectra for all the line candidates identified with the blind line search.

REFERENCES

Aravena, M., Decarli, R., Walter, F., et al. 2016a, ApJ, 833, 68 (Paper II)
Aravena, M., Decarli, R., Walter, F., et al. 2016b, ApJ, 833, 71 (Paper V)

Beckwith, S. V., Stiavelli, M., Koekemoer, A. M., et al. 2006, AJ, 132, 1729
Bell, E. F., McIntosh, D. H., Katz, N., & Weinberg, M. D. 2003, ApJL, 585, L117
Bolatto, A. D., Wolfire, M., & Leroy, A. K. 2013, ARA&A, 51, 207
Bouwens, R., Aravena, M., Decarli, R., et al. 2016, ApJ, 833, 72 (Paper VI)
Carilli, C., Chluba, J., Decarli, R., et al. 2016, ApJ, 833, 73 (Paper VII)
Carilli, C. L., & Walter, F. 2013, ARA&A, 51, 105
Chabrier, G. 2003, PASP, 115, 763
Coe, D., Benítez, N., Sánchez, S. F., et al. 2006, AJ, 132, 926
Daddi, E., Dannerbauer, H., Elbaz, D., et al. 2008, ApJ, 673, L21
da Cunha, E., Charlot, S., & Elbaz, D. 2008, MNRAS, 388, 1595
da Cunha, E., Groves, B., Walter, F., et al. 2013a, ApJ, 766, 13
da Cunha, E., Walter, F., Decarli, R., et al. 2013b, ApJ, 765, 9
da Cunha, E., Walter, F., Smail, I. R., et al. 2015, ApJ, 806, 110
Daddi, E., Dannerbauer, H., Liu, D., et al. 2015, A&A, 577, 46
Decarli, R., Walter, F., Aravena, M., et al. 2016a, ApJ, 833, 69 (Paper III)
Decarli, R., Walter, F., Aravena, M., et al. 2016b, ApJ, 833, 70 (Paper IV)
Decarli, R., Walter, F., Carilli, C., et al. 2014, ApJ, 782, 78
Ellis, R. S., McLure, R. J., Dunlop, J. S., et al. 2013, ApJL, 763, L7
Genzel, R., Burkert, A., Bouché, N., et al. 2008, ApJ, 687, 59
Genzel, R., Tacconi, L. J., Lutz, D., et al. 2015, ApJ, 800, 20
Giavalisco, M., Ferguson, H. C., Koekemoer, A. M., et al. 2004, ApJL, 600, L93
Grogin, N. A., Kocevski, D. D., Faber, S. M., et al. 2011, ApJS, 197, 35
Illingworth, G. D., Magee, D., Oesch, P. A., et al. 2013, ApJS, 209, 6
Koekemoer, A. M., Faber, S. M., Ferguson, H. C., et al. 2011, ApJS, 197, 36
Kurk, J., Cimatti, A., Daddi, E., et al. 2013, A&A, 549, 63
Le Fèvre, O., Vettolani, G., Garilli, B., et al. 2005, A&A, 439, 845
Lehmer, B. D., Brandt, W. N., Alexander, D. M., et al. 2005, ApJS, 161, 21
Madau, P., & Dickinson, M. 2014, ARA&A, 52, 415
Momcheva, I. G., Brammer, G. B., van Dokkum, P. G., et al. 2016, ApJS, 225, 27
Morris, A. M., Kocevski, D. D., Trump, J. R., et al. 2015, AJ, 149, 178
Oke, J. B., & Gunn, J. E. 1983, apj, 266, 713
Planck Collaboration XIII 2016, A&A, 594A, 13
Sargent, M. T., Daddi, E., Béthermin, M., et al. 2014, ApJ, 793, 19
Skelton, R. E., Whitaker, K. E., Momcheva, I. G., et al. 2014, ApJS, 214, 24
Tacconi, L. J., Genzel, R., Smail, I., et al. 2008, ApJ, 680, 246
Tacconi, L. J., Genzel, R., Neri, R., et al. 2010, Natur, 463, 781
Walter, F., Decarli, R., Carilli, C., et al. 2012, Natur, 486, 233
Walter, F., Decarli, R., Sargent, M., et al. 2014, ApJ, 782, 79
Weiß, A., Downes, D., Walter, F., & Henkel, C. 2007, ASPC, 375, 25
Williams, R. E., Blacker, B., Dickinson, M., et al. 1996, AJ, 112, 1335